Photochemical & Photobiological Sciences

PAPER

Cite this: *Photochem. Photobiol. Sci.*, 2016, **15**, 1012

Synergetic adsorption and photocatalytic degradation of pollutants over 3D TiO_2–graphene aerogel composites synthesized *via* a facile one-pot route†

Jing-Jie Zhang,[a] Yu-Hui Wu,[a] Jin-Ya Mei,[a] Guang-Ping Zheng,[b] Ting-Ting Yan,[a] Xiu-Cheng Zheng,*[a] Pu Liu[a] and Xin-Xin Guan*[a]

Received 2nd May 2016,
Accepted 27th June 2016

DOI: 10.1039/c6pp00133e

www.rsc.org/pps

A series of composites consisting of anatase TiO_2 nanocrystals and three-dimensional (3D) graphene aerogel (TiO_2–GA) were self-assembled directly from tetrabutyl titanate and graphene oxides *via* a one-pot hydrothermal process. TiO_2 was found to uniformly distribute inside the 3D network of GA in the resulting composites with large surface areas (S_{BET} > 125 m^2 g^{-1}) and high pore volumes (V_p > 0.22 cm^3 g^{-1}). In comparison with GA and TiO_2, the composites possessed much higher adsorption capacities and visible light photocatalytic activity in the degradation of rhodamine B (RhB). With an initial concentration of 20.0 mg L^{-1} of RhB, the adsorptive decolourization of RhB was as high as 95.1% and the total decolourization value reached up to 98.7% under visible light irradiation over 5.0 mg of the resulting composites. It was elucidated that the physical and chemical properties of the TiO_2–GA composites could be ascribed to their unique 3D nanoporous structure with high surface areas and the synergetic activities of graphene nanosheets and TiO_2 nanoparticles.

1. Introduction

Titanium dioxide (TiO_2) has attracted significant attention and has been well investigated because of its strong redox ability, long-term stability against photo-corrosion and chemical corrosion, relative nontoxicity, abundant availability, low cost and excellent optical and electrical properties.[1–3] However, the photocatalytic activities of TiO_2 are restricted by its low photocatalytic sensitivity in the UV region and the fast recombination of photogenerated electron–hole pairs.[4–6] In order to improve the photocatalytic performance of TiO_2, its optical absorption and charge transfer characteristics have to be optimized. It has been found that the incorporation of graphene or graphene oxides into TiO_2 could improve its photocatalytic performance.[7–9] Compared with two-dimensional (2D) graphene, three-dimensional (3D) graphene aerogel (GA) with nano-porous structures could be more capable of facilitating ion and mass transport. Hence in the composites containing TiO_2 and GA, GA is expected to facilitate the charge transfer, and ion and mass transfer involving TiO_2, thereby improving the photocatalytic performances of the composites.

As a bottom-up method, the self-assembly technique is one of the most effective strategies in implementing the practical applications of nanomaterials which are used as nanoscale building blocks to construct bulk materials.[10] Recently, TiO_2–graphene composites with 3D bulk forms such as hydrogels, aerogels or other macroscopic structures have been prepared by self-assembly methods.[1,3,4,11–14] Even so, to the best of our knowledge, there is no report on the one-pot self-assembly of 3D TiO_2–GA composites from tetrabutyl titanate (TBT) without a structure-directing agent.

In this work, 3D TiO_2–GA composites with various TiO_2 dosages were assembled from TBT and graphene oxides (GOs) *via* a one-pot hydrothermal process. The structural and chemical properties of the composites were characterized. The performances of the TiO_2–GA composites in pollutant abatement were investigated using rhodamine B (RhB) as the target dye.

2. Experimental methods

2.1. Preparation of TiO_2–GA composites

GO was prepared from natural graphite flakes with a modified Hummers' method reported previously.[15] The schematic of the

[a]*College of Chemistry and Molecular Engineering, Zhengzhou University, Zhengzhou 450001, China. E-mail: zhxch@zzu.edu.cn, guanxin@zzu.edu.cn*
[b]*Department of Mechanical Engineering, The Hong Kong Polytechnic University, Hung Hom, Kowloon, Hong Kong, China*

†Electronic supplementary information (ESI) available: DR UV-Vis spectra of pristine GA, TiO_2, and the TiO_2–GA(15) composites. See DOI: 10.1039/c6pp00133e

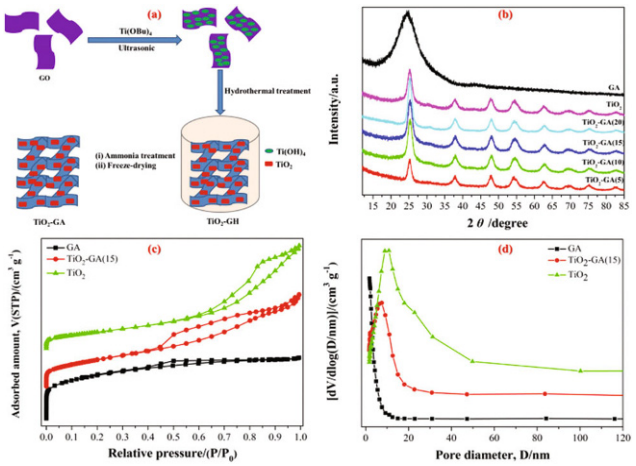

Fig. 1 Schematic of the self-assembly process of 3D TiO_2–GA composites (a); XRD patterns of the materials (b); N_2 adsorption–desorption isotherms (c) and pore size distributions (d) of GA, TiO_2–GA(15) and TiO_2.

synthetic route leading to TiO_2–GA is illustrated in Fig. 1a. In brief, 17.5 mL of absolute ethanol was added to 17.5 mL of the GO solution (3.6 mg mL^{-1}) and sonicated for 1 h. A predesigned amount of TBT was added dropwise and the reactant was sonicated for another 1 h. Subsequently, the mixture was transferred into a 50 mL Teflon-lined stainless-steel autoclave and maintained at 180 °C for 24 h. The resulting TiO_2–graphene hydrogels (TiO_2–GH) were hydrothermally treated in ammonia solution (10 v/v%) at 120 °C for 3 h, following by a freeze-drying process. The resulting composites were denoted TiO_2–GA(X) where X = 5, 10, 15, 20 represent the mass ratio of TBT to GO. For comparison, GA and TiO_2 were prepared with the same procedure without the addition of TBT and GOs, respectively.

2.2. Structural characterization

The porous nature of the samples was investigated by the nitrogen adsorption–desorption isotherm at −196 °C recorded on a Micromeritics ASAP 2420 surface area and porosity analyzer. The specific surface area was calculated from the nitrogen adsorption isotherm within the relative pressure range of 0.05–0.25 by the Brunauer–Emmett–Teller (BET) method. The microscopic features of the TiO_2–GA materials were examined using a Zeiss Ultra 55 scanning electron microscope (SEM) and a JEM-2100 high-resolution transmission electron microscope (HRTEM). Phase structures of the as-synthesized samples were characterized by X-ray diffraction (XRD) using a Panalytical X'pertPro diffractometer, which was operated at 40 kV and 40 mA and with Cu Kα radiation (λ = 0.154 nm). Studies on surface chemistry were conducted by X-ray photoelectron spectroscopy (XPS) using an RBD upgraded PHI-5000C ESCA system (Perkin Elmer) with Al Kα radiation ($h\nu$ = 1486.6 eV). The binding energies were calibrated using containment carbon (C 1s = 284.6 eV). Raman spectra were recorded on a Renishaw RM-1000 spectrometer and diffuse reflectance ultraviolet-visible (DR UV-Vis) spectra were recorded using a Varian Cary 5000 UV-Vis-NIR spectrophotometer with a $BaSO_4$ reference. Fourier-transform infrared (FT-IR) spectra were recorded on a Thermo Scientific Nicolet 380 Fourier transform spectrometer using a KBr pellet technique to characterize the samples.

2.3. Adsorbing and photocatalytic measurements on TiO_2–GA

The adsorbing and visible light driven photocatalytic activities of the samples were measured by monitoring the adsorption and degradation performance of RhB at room temperature. In each experiment, the slurry containing 5.0 mg of catalyst and 25 mL of 20.0 mg L^{-1} organic dye solution was stirred in a cylindrical quartz vessel in a dark environment to detect the adsorption capacity. The overall removal performance was monitored when the irradiation of a 300 W Xe lamp was applied, where the UV light (λ < 420 nm) had been blocked by using a cut-off filter. At a given time interval, the samples of the reaction solution were taken out and the suspension was filtered to obtain a clear solution of the dye. Then, the residual concentration of organic dyes was measured by UV-Vis absorption analysis, and the peak absorbance of RhB at 552 nm was used to determine its concentration. The efficiency of RhB removal was calculated by eqn (1):

$$\text{Decolourization}\,(\%) = \frac{C_0 - C}{C_0} \times 100 \qquad (1)$$

where C_0 = 20.0 mg L^{-1} is the initial concentration of RhB and C is the concentration of RhB at various time intervals.

3. Results and discussion

The crystalline phases of GA, TiO_2 and the TiO_2–GA composites were investigated by XRD patterns, as shown in Fig. 1b. The sharp diffraction peaks that appeared in the XRD patterns for TiO_2 and the TiO_2–GA composites at 2θ = 25.3°, 37.8°, 48.0°, 53.5°, 55.6°, 62.7°, 69.7°, 75.1° and 82.7° can be perfectly assigned to the (1 0 1), (0 0 4), (2 0 0), (1 0 5)/(2 1 1), (2 0 0), (2 0 4), (1 1 6)/(2 2 0), (1 1 5) and (3 0 3) planes of the anatase structure, respectively, which is the most photoactive crystalline phase in TiO_2.[16–19] On the other hand, the disappearance of the characteristic peak of the (0 0 2) plane for GA at *ca.* 24.8° in the XRD patterns for the TiO_2–GA composites could be explained by the low GA content and the overlapping or screening caused by the strong (1 0 1) peak for TiO_2. As shown in Table 1, the average crystal size decreases from 7.5 nm for the pure TiO_2 to about 5.7–6.7 nm for the TiO_2–GA composites mainly because the incorporation of GA promotes the nucleation of TiO_2 nanoparticles.

Fig. 1c shows that the N_2 adsorption and desorption branches of TiO_2 step occurs at a relative pressure (P/P_0) of about 0.55–1.00, indicating that the pores mainly result from the mesopores and the voids among the nanoparticles. On the other hand, compared to the weak capillary condensation for GA which occurs at P/P_0 = 0.35–0.75, the isotherm of TiO_2–GA (15) is typically of type IV with an H1 hysteresis loop (P/P_0 =

Table 1 Textural and structural characteristics of GA, TiO_2, and the TiO_2–GA composites

Sample	S_{BET} [a] ($m^2\ g^{-1}$)	V_p [b] ($cm^3\ g^{-1}$)	D_a [c] (nm)	D_a [d] (nm)	D_a [e] (nm)	TiO_2 crystal size[f] (nm)
TiO_2	152.8	0.381	9.98	8.05	7.26	7.5
TiO_2–GA(20)	125.7	0.222	7.07	6.44	5.93	6.7
TiO_2–GA(15)	234.6	0.341	5.81	5.35	4.70	6.6
TiO_2–GA(10)	283.6	0.278	3.92	3.83	3.62	5.7
TiO_2–GA(5)	409.0	0.512	5.01	3.87	3.53	5.7
GA	379.1	0.228	2.40	2.91	3.02	—

[a] S_{BET}, BET surface area. [b] V_p, single point adsorption total pore volume. [c] D_a, adsorption average pore width ($4V/A$ by BET). [d] D_a, BJH adsorption average pore diameter ($4V/A$). [e] D_a, BJH desorption average pore diameter ($4V/A$). [f] The average crystal size was estimated from XRD line-broadening of anatase TiO_2 at the (1 0 1) diffraction peak according to Scherrer's equation.

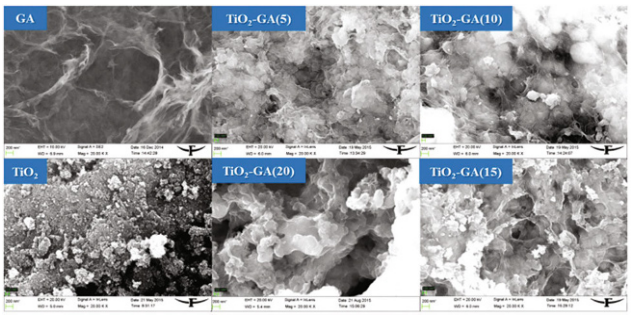

Fig. 2 SEM images of GA, TiO_2 and the TiO_2–GA composites.

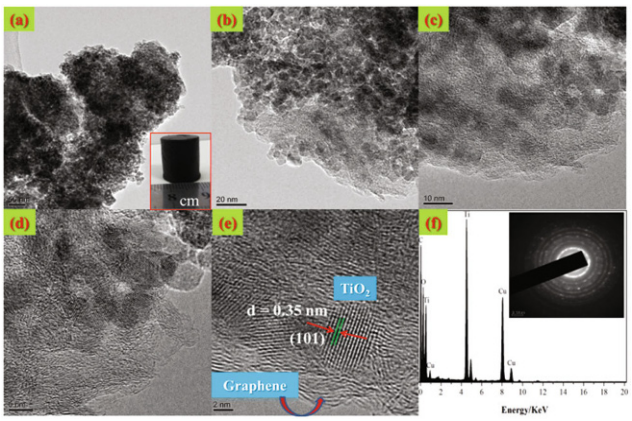

Fig. 3 TEM images with different magnifications (a–e), photograph (inset in a), EDX spectrum (f) and SAED patterns (inset in f) of the TiO_2–GA(10) composite.

0.35–0.95), suggesting that it has a mesoporous structure.[20] As shown in Fig. 1d, both GA and TiO_2–GA(15) display a much narrower pore size distribution in comparison with that of TiO_2. Furthermore, the pore size of TiO_2–GA(15) is obviously larger than that of GA due to the incorporation of TiO_2 nanoparticles, as listed in Table 1. Except for TiO_2–GA(20), the TiO_2–GA composites have higher specific surface area than that of TiO_2 (S_{BET} = 152.8 $m^2\ g^{-1}$), which is attributed to the unique 3D framework of GA. Among the TiO_2–GA composites, TiO_2–GA(5) exhibits the highest specific surface area (S_{BET} = 409.0 $m^2\ g^{-1}$) and total pore volume (V_p = 0.512 $cm^3\ g^{-1}$) among the resulting composites, which are even higher than those of GA (S_{BET} = 379.1 $m^2\ g^{-1}$) and TiO_2 (V_p = 0.381 $cm^3\ g^{-1}$). The ultra-high S_{BET} and V_p of TiO_2–GA(5) could be caused by the synergetic effects of the assembled graphene nanosheets and TiO_2 nanoparticles. Those highly dispersed TiO_2 nanoparticles act as spacers to prevent the aggregation of graphene nanosheets, which further increase the specific surface area of GA. TiO_2–GA(20) exhibits the lowest surface area and pore volume (S_{BET} = 125.7 $m^2\ g^{-1}$, V_p = 0.222 $cm^3\ g^{-1}$), which may be ascribed to the serious aggregation of TiO_2 in GA or the TiO_2 nanoparticles blocking the pores of GA. The unique properties such as high surface area and narrow mesoporous structure of the TiO_2–GA composites would be very helpful to enhance their performance in the removal of organic dyes.

The morphology and structure of the materials are characterized by SEM and TEM (Fig. 2 and 3). As shown in Fig. 2, the TiO_2–GA composites retain the well-defined and interconnected 3D porous network of GA with pore sizes ranging from sub-micrometers to several micrometers, which could result from the overlapping or coalescing of graphene nanosheets.[21] Meanwhile, the TiO_2 nanoparticles are anchored uniformly on the surfaces of graphene nanosheets or wrapped by the graphene nanosheets in the TiO_2–GA composites, suggesting the efficient assembly of TiO_2 nanoparticles and graphene nanosheets during the one-pot synthesis process. In the TiO_2–GA composites with high TiO_2 dosage such as TiO_2–GA(20), aggregation of TiO_2 nanoparticles can be observed, which is consistent with those results of XRD and N_2 adsorption–desorption analysis.

The typical TEM images demonstrate that the graphene nanosheets in TiO_2–GA(10) are homogeneously covered with TiO_2 with a size of around 5–7 nm (Fig. 3a–d), which is in agreement with that determined by XRD. The high resolution TEM images further reveal that the crystal lattice fringe is 0.35 nm (Fig. 3e), corresponding to the (1 0 1) plane of anatase TiO_2.[22–24] As shown in Fig. 3f, energy dispersive spectroscopy (EDX) reveals the presence of titanium, oxygen, copper and carbon elements in the TiO_2–GA(10) sample. The content of copper is from the copper grid which is used in the TEM analysis. As shown in the inset of Fig. 3f, the SAED patterns confirm the crystalline nature of TiO_2. Moreover, the SAED ring patterns corresponding to the (1 0 1), (0 0 4), (2 0 0), (1 0 5), and (2 0 4) lattice planes also indicate the presence of TiO_2 with the anatase phase. The SEM and TEM results thus well demonstrate the incorporation of TiO_2 into GA during the hydrothermal process. The results further demonstrate that the TiO_2 nanoparticles possess a high crystallinity in the composites. Such highly crystallized nanostructures could improve the photocatalytic performance of TiO_2 since they may reduce the opportunity of charge recombination.[25] Remarkably, the

typical composites display a cylindrical shape (inset of Fig. 3a) which is similar to that of GA with an ultralight characteristic,[26] indicating that the TiO_2–GA composites retain the 3D monolithic architecture of GA. Such 3D graphene-based aerogel embedded with nanoparticles may enhance the interfacial contacts and suppress the dissolution and agglomeration among the nanoparticles, thereby improves the photoelectrochemical activities and stability of the hybrids.[27]

Fig. 4a shows the FT-IR spectra of GA, TiO_2 and the TiO_2–GA composites. The C═O and C–O stretching vibration bands at 1725 cm^{-1} and 1045 cm^{-1} for COOH groups almost disappear in the spectra for GA and the TiO_2–GA composites, indicating that the COOH groups of GO are reduced during the solvothermal process. For TiO_2 and the TiO_2–GA composites, the broad absorption below 1000 cm^{-1} is presumably ascribed to the combination of Ti–O–Ti and Ti–O–C vibration modes resulting from the chemical interaction between TiO_2 and graphene.[28] Moreover, the absorption peak at around 1600 cm^{-1} attributed to the skeletal vibration of graphene becomes wider and shifts slightly to higher wavenumbers with increasing TiO_2 dosage, resulting from its overlapping with the absorption band at 1633 cm^{-1} for Ti–O–Ti stretching vibration.[29]

Fig. 4b shows the Raman spectra for GA, TiO_2 and the TiO_2–GA composites. There are two bands at about 1330 and 1590 cm^{-1} in the spectrum for GA, corresponding to the disordered (D) band and graphitic (G) band, respectively. The D band suggests the presence of sp^3 defects in carbon. The G band is common to the sp^2 carbon atoms and provides information on the in-plane vibration of sp^2 bonded carbon atoms.[15,30] The spectrum for TiO_2 reveals the typical Raman modes for anatase TiO_2 such as B_{1g}, (A_{1g} + B_{1g}) and E_g corresponding to the characteristic bands at about 398, 515, and 639 cm^{-1}.[31] The anatase TiO_2 is consistent with the crystal structure determined by XRD. Furthermore, it can be found that the intensities of these bands increase with increasing TiO_2 dosage in the TiO_2–GA composites. As for TiO_2–GA(5), these bands could not be detected because of the low dosage of TiO_2 and the dilution of ultralight GA. The intensity ratio of I_D/I_G remains constant (~1.20) for the composites which suggests the incorporation of TiO_2 has no obvious effect on the defects and disorders in the graphitized structures of GA.

As shown in Fig. 4c, the XPS survey scan for TiO_2–GA(10) confirms the presence of the elements C, O, N, and Ti. The molar ratios of C, O, N, and Ti are 63.20 : 29.36 : 1.02 : 6.43. The O/Ti ratio is higher than that of the stoichiometry of TiO_2 due to the additional oxygen atoms detected in the functional groups of GA. The peaks at 284.6, 286.6, 287.6 and 289.4 eV in the high-resolution C 1s XPS spectrum could be assigned to the C═C/C–C bond in the aromatic rings, the C–O bond resulting from the overlapping of C–O–C and C–OH (C–O of epoxy), C═O and O–C═O groups, respectively. The peak at 286.0 eV is assigned to C–N groups.[15] As shown in Fig. 4d, the very low intensity of the peak for O–C═O groups also indicates that GO is efficiently reduced into graphene after the hydrothermal treatment. The N element could result from the ammonia solution used in the pretreatment of TiO_2–GA composites before freeze drying. As shown in Fig. 4e, the deconvoluted N 1s spectrum shows three main peaks centered at 398.9 eV (pyridine N), 400.1 eV (pyrrolic N) and 401.2 eV (graphitic N).[26] In the Ti 2p spectrum shown in Fig. 4f, there are doublet peaks of Ti $2p_{1/2}$ (B.E. ~ 459.2 eV) and Ti $2p_{3/2}$ (B.E. ~ 464.9 eV), indicating the Ti^{4+} valence state in the composites.[19]

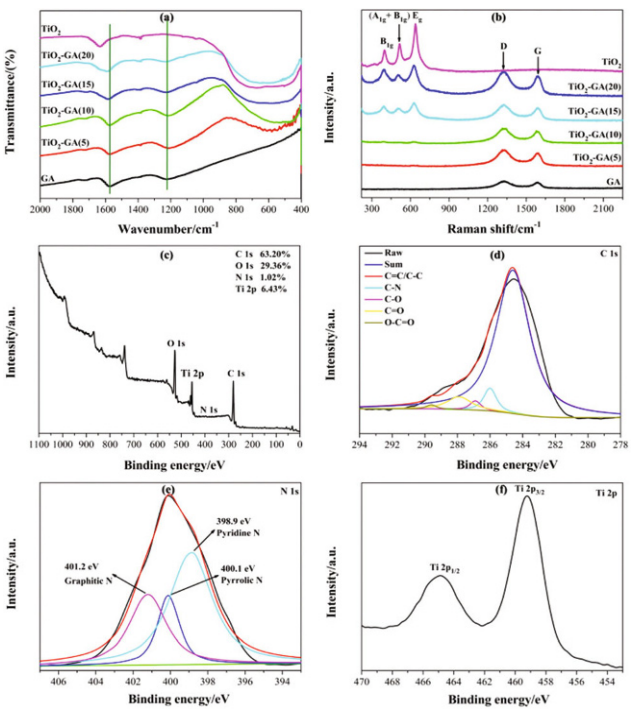

Fig. 4 FT-IR (a) and Raman (b) spectra of GA, TiO_2, and the TiO_2–GA composites; XPS survey spectrum (c), high-resolution C 1s spectrum (d), high-resolution N 1s (e) and high-resolution Ti 2p spectrum (f) for the TiO_2–GA(10) composites.

The influence of GA on the bandgap energy of TiO_2 is studied by DR UV-vis measurements on the TiO_2–GA composites. Fig. S1† shows the DR UV-Vis spectra for GA, TiO_2, and the TiO_2–GA(15) composite. The slight response in the range of 200–400 nm for TiO_2 may be attributed to the transition of O 2p → Ti 3d. As for TiO_2–GA(15), an obvious wide band appeared within a higher range of 400–800 nm. This may be caused by the hybridization of C 2p and O 2p atomic orbits in the formation of a new valence band (Ti–O–C bond), similar to the case of P25–graphene composites.[32] It is indicative that the bandgap energy is reduced in the TiO_2–GA composites, which could be beneficial for the efficiency of photocatalysis of the composites under visible light irradiation.

The dye-contaminated wastewater released from textile, painting, leather, printing and photography industries becomes one of the most serious environmental problems. The wastewater could be purified *via* adsorption and photocatalytic degradation of the dyes. 3D GA has been considered as an ideal adsorbent for water purification.[33] RhB, herein, is selected as the target dye to investigate the adsorption capability of the TiO_2–GA composites. As shown in Fig. 5 and 7a,

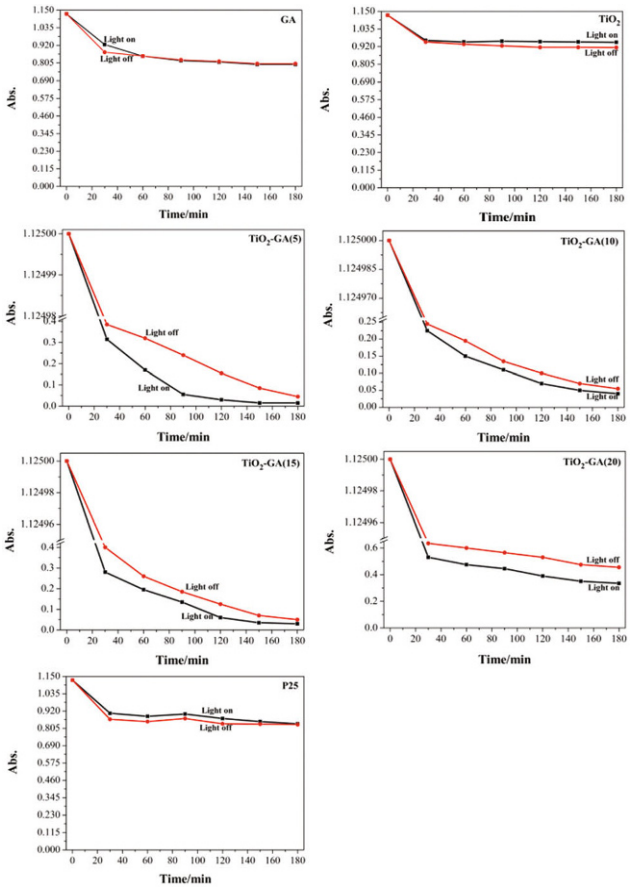

Fig. 5 The variations of absorbance for RhB dye over the resulting materials and P25 with and without visible light irradiation.

the decolourization value ascribed to the adsorption of the dye increases greatly in the time range of 0 to 30 min and then increases slowly. Under the present harsh conditions (25 mL of 20.0 mg L^{-1} RhB solution, 5.0 mg of adsorbent), the finial decolourization value is 28.9% over GA, which is higher than that of TiO_2 (18.8%). The resulting TiO_2–GA composites exhibit much superior adsorption capability to GA and TiO_2, among them, TiO_2–GA(10) shows the strongest adsorptivity in 180 min. The final decolourization value is about 96% over those composites except for TiO_2–GA(20). Even so, the value of TiO_2–GA(20) (59.6%) is still much higher than that of TiO_2 (15–35%, under the conditions of 30 mg adsorbent and 50 mL of 10 mg L^{-1} RhB)[34] and the TiO_2–graphene composites (15–25%, under the conditions of 100 mg adsorbent and 100 mL of 1.25×10^{-4} mol L^{-1} RhB).[35] The excellent adsorption capability can be attributed to the unique 3D porous structure and large hydrophobic surface area of GA and to the abundant amount of TiO_2 nanoparticles embedded on the graphene nanosheets, which increase the surface roughness and optimize the porous structure of TiO_2–GA. In addition, the selective adsorption of the aromatic dye on the aromatic regions of GA by π–π electron coupling may also enhance the adsorptivity of TiO_2–GA.[36] However, the specific surface area and the adsorptivity of TiO_2–GA are reduced if too many TiO_2 nanoparticles are incorporated into GA. That's why TiO_2–GA (20) with the highest TiO_2 content exhibits the lowest adsorption capability.

It is expected that a hybrid consisting of photocatalysts and graphene could have outstanding synergetic photocatalytic efficiency.[19,24,32,37–42] According to the previous studies[19,36] which focused on 2D TiO_2–graphene composite photocatalysts, the improvement of photocatalytic activities can be explained as follows: (a) graphene with a π-conjugated planar structure can increase dye absorption through π–π stacking; (b) the unpaired π electrons of graphene can reduce the bandgap of the photocatalyst because of its doping effect on the band structures of TiO_2, which enhances the absorption of visible light; and (c) graphene which has excellent charge mobility, provides conductive electron channels for the separation of electrons, resulting in the inhibition of recombination of electrons and holes. As for the TiO_2–GA composites, 3D GA not only maintains the chemical bonds and structural characteristics of graphene but also has abundant macro-pores. The porosity would improve the utilization of visible light since the visible light entering the pores can be repeatedly reflected until it is completely absorbed. Moreover, 3D GA with large surface areas may adsorb more RhB molecules than 2D graphene and TiO_2, leading to the enhanced photocatalytic efficiency. Hence, TiO_2–GA composites achieve an excellent synergetic effect of photocatalytic activities of TiO_2 and GA and their photocatalytic efficiency could be enhanced.

As shown in Fig. 6, GA facilitates the transfer of photogenerated electrons, which could expand the light absorption range and suppress the electron–hole recombination. When the system is under visible light irradiation, the valence band (VB) electrons of the TiO_2 semiconductor are excited to the conduction bands (CB), leaving holes in the VB, thereby forming photo-induced electron–hole pairs. Those holes are able to react with water to form reactive oxygen species ($OH^{\bullet}$). Furthermore, e^- transferring to graphene aerogel would react with O_2 on the surfaces of catalysts to form $O_2^{\bullet-}$, which could damage or degrade the organic dyes.

As shown in Fig. 5 and 7a, the adsorption performance of the TiO_2–GA composites will not be equilibrated within 3 h

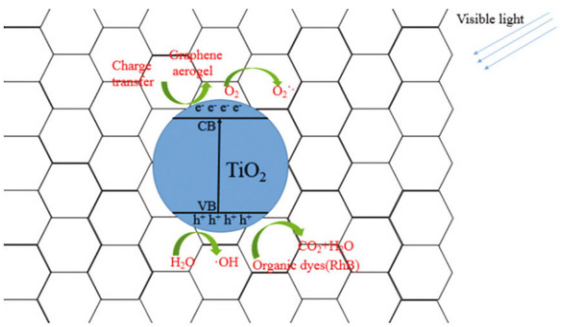

Fig. 6 Schematic of possible mechanisms for the photocatalytic degradation of RhB over the TiO_2–GA composites under visible light irradiation.

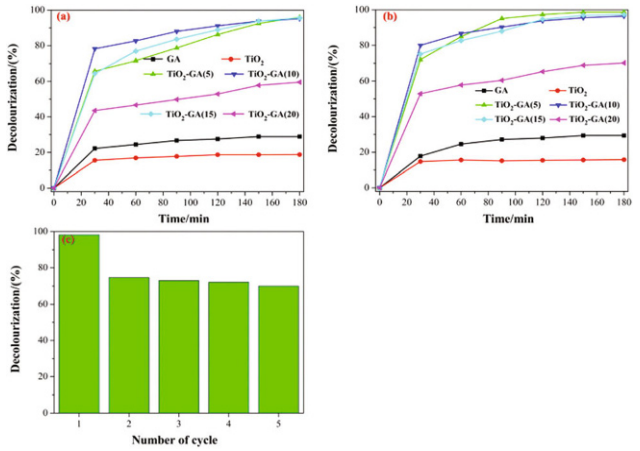

Fig. 7 Adsorptive performance (a) and total removal performance (b) of the catalysts for RhB dye under visible light irradiation; (c) stability of the typical TiO_2–GA(5) composites for the removal of RhB.

under the present conditions, suggesting that the decolourization of RhB is determined by both adsorption and photocatalytic degradation over the materials under visible light irradiation (Fig. 7b). As shown in Fig. 5, the decolourization values for TiO_2 and P25 under visible light irradiation are lower than that under the dark conditions, indicating that visible light irradiation has a negative effect on the removal of RhB over them. However, the TiO_2–GA composites show obviously higher decolourization values under visible light irradiation than that under the dark conditions, implying that the incorporation of GA indeed increases the photocatalytic activity of TiO_2 under visible light irradiation. Among those composites, TiO_2–GA(5) exhibits the best performance of RhB removal and the final decolourization value is as high as 98.7% due to the active adsorptive and photocatalytic sites, which could be ascribed to its optimized structural characteristics (S_{BET} = 409.0 m^2 g^{-1}, V_p = 0.512 cm^3 g^{-1}) and the best dispersion of TiO_2 nanoparticles inside GA.

The TiO_2–GA(5) composite is used to further investigate the reusability of the composites. The solid catalysts separated from the RhB solution are washed with water and dried at 110 °C prior to the next cycle of reaction. The operation conditions are 0.4 mg of catalysts per mL of RhB solution and irradiation for 30 min using a 300 W Xe lamp. As shown in Fig. 7c, after five successive cycles, decolourization is still as high as 70.0%. The results imply that the TiO_2–GA composites are efficient in the removal of organic dyes.

4. Conclusions

For the first time a one-pot hydrothermal method combined with freeze drying was developed to fabricate 3D TiO_2–graphene aerogel (TiO_2–GA) composites without using any structure-directing agent. The results indicated that the TiO_2–GA composites exhibited excellent adsorption capacities and visible light photocatalytic activity in the degradation of rhodamine B. Among the composites, TiO_2–GA(10) exhibited the highest adsorptivity and TiO_2–GA(5) exhibited the best total removal performance. The results demonstrated that the TiO_2–GA composites synthesized by the one-pot self-assembly method could be used as highly efficient adsorbents and photocatalysts for pollutant abatement.

Acknowledgements

The authors are grateful for the support of the National Natural Science Foundation of China (no. U1304203 & J1210060), the Foundation of He'nan Educational Committee (no. 16A150046) and the Innovation Foundation of Zhengzhou University (no. 201610459062 and 2016xjxm251). GPZ is grateful for the support provided by the Science and Technology Innovation Commission of Shenzhen, China (no. JCYJ2013041152508657).

Notes and references

1 W. Yan, F. He, S. L. Gai, P. Gao, Y. J. Chen and P. P. Yang, A novel 3D structured reduced graphene oxide/TiO_2 composite: synthesis and photocatalytic performance, *J. Mater. Chem. A*, 2014, **2**, 3605–3612.

2 P. Zhang, T. Tachikawa, M. Fujitsuka and T. Majima, Efficient charge separation on 3D architectures of TiO_2 mesocrystals packed with a chemically exfoliated MoS_2 shell in synergetic hydrogen evolution, *Chem. Commun.*, 2015, **51**, 7187–7190.

3 Y. Agrawal, G. Kedawat, P. Kumar, J. Dwivedi, V. N. Singh, R. K. Gupta and B. K. Gupta, High-performance stable field emission with ultralow turn on voltage from rGO conformal coated TiO_2 nanotubes 3D arrays, *Sci. Rep.*, 2015, **5**, 11612.

4 W. J. Han, C. Zang, Z. Y. Huang, H. Zhang, L. Ren, X. Qi and J. X. Zhong, Enhanced photocatalytic activities of three-dimensional graphene-based aerogel embedding TiO_2 nanoparticles and loading MoS_2 nanosheets as Co-catalyst, *Int. J. Hydrogen Energy*, 2014, **39**, 19502–19512.

5 A. L. Linsebigler, G. Lu and J. T. Yates, Photocatalysis on TiO_2 surfaces: principles, mechanisms, and selected results, *Chem. Rev.*, 1995, **95**, 735–758.

6 F. J. Wu, W. Liu, J. L. Qiu, J. Z. Li, W. Y. Zhou, Y. P. Fang, S. T. Zhang and X. Li, Enhanced photocatalytic degradation and adsorption of methylene blue via TiO_2 nanocrystals supported on graphene-like bamboo charcoal, *Appl. Surf. Sci.*, 2015, **358**, 425–435.

7 L. L. Tan, W. J. Ong, S. P. Chai, B. T. Goh and A. R. Mohamed, Visible-light-active oxygen-rich TiO_2 decorated 2D graphene oxide with enhanced photocatalytic activity toward carbon dioxide reduction, *Appl. Catal., B*, 2015, **179**, 160–170.

8 W. G. Wang, J. G. Yu, Q. J. Xiang and B. Cheng, Enhanced photocatalytic activity of hierarchical macro/mesoporous TiO_2-graphene composites for photodegradation of acetone in air, *Appl. Catal., B*, 2012, **120**, 109–116.

9 M. Aleksandrzak, P. Adamski, W. Kukulka, B. Zielinska and E. Mijowska, Effect of graphene thickness on photocatalytic activity of TiO_2-graphene nanocomposites, *Appl. Surf. Sci.*, 2015, **331**, 193–199.

10 S. Man, Self-assembly and transformation of hybrid nano-objects and nanostructures under equilibrium and non-equilibrium conditions, *Nat. Mater.*, 2009, **8**, 781–792.

11 Z. Y. Zhang, F. Xiao, Y. L. Guo, S. Wang and Y. Q. Liu, One-pot self-assembled three-dimensional TiO_2-graphene hydrogel with improved adsorption capacities and photocatalytic and electrochemical activities, *ACS Appl. Mater. Interfaces*, 2013, **5**, 2227–2233.

12 B. C. Qiu, M. Y. Xing and J. L. Zhang, Mesoporous TiO_2 nanocrystals grown in situ on graphene aerogels for high photocatalysis and lithium-ion batteries, *J. Am. Chem. Soc.*, 2014, **136**, 5852–5855.

13 X. Jiang, X. L. Yang, Y. H. Zhu, H. L. Jiang, Y. F. Yao, P. Zhao and C. Z. Li, 3D nitrogen-doped graphene foams embedded with ultrafine TiO_2 nanoparticles for high performance lithium-ion batteries, *J. Mater. Chem. A*, 2014, **2**, 11124–11133.

14 F. H. Zhao, B. H. Dong, R. J. Gao, G. Su, W. Liu, L. Shi, C. H. Xia and L. X. Cao, A three-dimensional graphene-TiO_2 nanotube nanocomposite with exceptional photocatalytic activity for dye degradation, *Appl. Surf. Sci.*, 2015, **351**, 303–308.

15 J. K. Meng, Y. Cao, Y. Suo, Y. S. Liu, J. M. Zhang and X. C. Zheng, Facile fabrication of 3D SiO_2@graphene aerogel composites as anode material for lithium ion batteries, *Electrochim. Acta*, 2015, **176**, 1001–1009.

16 G. Cheng, M. S. Akhtar, O. B. Yang and F. J. Stadler, Novel preparation of anatase TiO_2@reduced graphene oxide hybrids for high-performance dye-sensitized solar cells, *ACS Appl. Mater. Interfaces*, 2013, **5**, 6635–6642.

17 C. Chen, W. M. Cai, M. Long, B. X. Zhou, Y. H. Wu, D. Y. Wu and Y. J. Feng, Synthesis of visible-Light responsive graphene oxide/TiO_2 composites with p/n heterojunction, *ACS Nano*, 2010, **4**, 6425–6432.

18 K. R. Parmar, S. Basha and Z. V. P. Murthy, Application of graphene oxide as a hydrothermal catalyst support for synthesis of TiO_2 whiskers, *Chem. Commun.*, 2014, **50**, 15010–15013.

19 K. M. Cho, K. H. Kim, H. O. Choi and H. T. Jung, A highly photoactive, visible-light-driven graphene/2D mesoporous TiO_2 photocatalyst, *Green Chem.*, 2015, **17**, 3972–3978.

20 B. Yu, X. S. Jiang and J. Yin, Silica/titania sandwich-like mesoporous nanosheets embedded with metal nanoparticles templated by hyperbranched poly(ether amine) (hPEA), *Nanoscale*, 2013, **5**, 5489–5498.

21 C. Li and G. Shi, Three-dimensional graphene architectures, *Nanoscale*, 2012, **4**, 5549–5563.

22 W. Li, F. Wang, Y. P. Liu, J. X. Wang, J. P. Yang, L. J. Zhang and A. A. Elzatahry, General strategy to synthesize uniform mesoporous TiO_2/graphene/mesoporous TiO_2 sandwich-like nanosheets for highly reversible lithium storage, *Nano Lett.*, 2015, **15**, 2186–2193.

23 S. L. Yang, C. Y. Cao, P. P. Huang, L. Peng, Y. B. Sun, F. Wei and W. G. Song, Sandwich-like porous TiO_2/reduced graphene oxide (rGO) for high-performance lithium-ion batteries, *J. Mater. Chem. A*, 2015, **3**, 8701–8705.

24 S. Thakur and N. Karak, Tuning of sunlight-induced self-cleaning and selfhealing attributes of an elastomeric nanocomposite by judicious compositional variation of the TiO_2-reduced graphene oxide nanohybrid, *J. Mater. Chem. A*, 2015, **3**, 12334–12342.

25 H. B. Wu, H. H. Hng and X. W. D. Lou, Direct synthesis of anatase TiO2 nanowires with enhanced photocatalytic activity, *Adv. Mater.*, 2012, **24**, 2567–2571.

26 J. K. Meng, Y. Suo, J. Li, G. P. Zheng, Y. S. Liu, J. M. Zhang and X. C. Zheng, Nitrogen-doped graphene aerogels as anode materials for lithium-ion battery: Assembly and electrochemical properties, *Mater. Lett.*, 2015, **160**, 392–396.

27 Z. S. Wu, S. Yang, Y. Sun, K. Parvez, X. Feng and K. Mùllen, 3D nitrogen-doped graphene aerogel-supported Fe_3O_4 nanoparticles as efficient electrocatalysts for the oxygen reduction reaction, *J. Am. Chem. Soc.*, 2012, **134**, 9082–9085.

28 A. J. Wang, W. Yu, Y. Fang, Y. L. Song, D. Jia, L. L. Long, M. P. Cifuentes, M. G. Humphrey and C. Zhang, Facile hydrothermal synthesis and optical limiting properties of TiO_2-reduced graphene oxide Nanocomposites, *Carbon*, 2015, **89**, 130–141.

29 H. Liu, X. Dong, X. Wang, C. Sun, J. Li and Z. Zhu, A green and direct synthesis of graphene oxide encapsulated TiO_2 core/shell structures with enhanced photoactivity, *Chem. Eng. J.*, 2013, **230**, 279–285.

30 W. Q. Li, X. Liu and H. X. Li, Hydrothermal synthesis of graphene/Fe^{3+}-doped TiO_2 nanowire composites with highly enhanced photocatalytic activity under visible light irradiation, *J. Mater. Chem. A*, 2015, **3**, 15214–15224.

31 T. Ohsaka, F. Izumi and Y. Fujiki, Raman spectrum of anatase, TiO_2, *J. Raman Spectrosc.*, 1978, **7**, 321–324.

32 H. Zhang, X. J. Lv, Y. M. Li, Y. Wang and J. H. Li, P25-graphene composite as a high performance photocatalyst, *ACS Nano*, 2010, **4**, 380–386.

33 Z. Han, Z. H. Tang, S. L. Shen, B. Zhao, G. P. Zheng and J. H. Yang, Strengthening of graphene aerogels with tunable density and high adsorption capacity towards Pb^{2+}, *Sci. Rep.*, 2014, **4**, 5025.

34 L. X. Zhang, J. Zhang, H. F. Jiu, C. H. Ni, X. Zhang and M. L. Xu, Graphene-based hollow TiO_2 composites with enhanced photocatalytic activity for removal of pollutants, *J. Phys. Chem. Solids*, 2015, **86**, 82–89.

35 D. Maruthamani, D. Divakar and M. Kumaravel, Enhanced photocatalytic activity of TiO_2 by reduced graphene oxide

in mineralization of Rhodamine B dye, *J. Ind. Eng. Chem.*, 2015, **30**, 33–43.

36 H. Zhang, X. J. Lv, Y. M. Li, Y. Wang and J. H. Li, P25-graphene composite as a high performance photocatalyst, *ACS Nano*, 2010, **4**, 1380–1386.

37 Y. Wang, Z. Li, Y. He, F. Li, X. Q. Liu and J. B. Yang, Low-temperature solvothermal synthesis of graphene–TiO2 nanocomposite and its photocatalytic activity for dye degradation, *Mater. Lett.*, 2014, **134**, 115–118.

38 C. Xu, J. L. Zhu, R. S. Yuan and X. Z. Fu, More effective use of graphene in photocatalysis by conformal attachment of small sheets to TiO_2 spheres, *Carbon*, 2016, **96**, 394–402.

39 P. Muthirulan, C. NirmalaDevi and M. Meenakshi Sundaram, A green approach to the fabrication of titania–graphene nanocomposites: Insights relevant to efficient photodegradation of Acid Orange 7 dye under solar irradiation, *Mater. Sci. Semicond. Process.*, 2014, **25**, 219–230.

40 Y. R. Li, J. Yan, Q. Su, E. Q. Xie and W. Lan, Preparation of graphene-TiO_2 nanotubes/nanofibers composites as an enhanced visible light photocatalyst using a hybrid synthetic strategy, *Mater. Sci. Semicond. Process.*, 2014, **27**, 695–701.

41 H. Y. Xia, G. Q. He, Y. L. Min and T. Liu, Role of the crystallite phase of TiO_2 in graphene/TiO_2 photocatalysis, *J. Mater. Sci: Mater. Electron.*, 2015, **26**, 3357–3363.

42 P. H. Shao, J. Y. Tian, W. X. Shi, S. S. Gao and F. Y. Cui, Eco-friendly one-pot synthesis of ultradispersed TiO_2 nanocrystals/graphene nanocomposites with high photocatalytic activity for dye degradation, *J. Mater. Chem. A*, 2015, **3**, 19913–19919.